Applied Surface Science 412 (2017) 58–68

Contents lists available at ScienceDirect

Applied Surface Science

journal homepage: www.elsevier.com/locate/apsusc

Full Length Article

Enhanced photocatalytic properties of ZnO/reduced graphene oxide sheets (rGO) composites with controllable morphology and composition

Yanting Zhao, Lin Liu, Tingting Cui, Guoxiu Tong*, Wenhua Wu

College of Chemistry and Life Sciences, Zhejiang Normal University, Jinhua 321004, People's Republic of China

ARTICLE INFO

Article history:
Received 12 February 2017
Received in revised form 22 March 2017
Accepted 23 March 2017
Available online 27 March 2017

Keywords:
ZnO/rGO composite
Chemical etching method
Optical property
Size- and composition-dependent photocatalytic property

ABSTRACT

ZnO with various morphologies and contents was used to decorate reduced graphene oxide (rGO) sheets via an easy one-step low-temperature chemical etching route to improve photocatalytic properties. The ZnO shape and content in ZnO/rGO composites were adjusted by changing aging time, heating mode, and rGO mass added. Shape and content-dependent optical and photocatalytic properties are observed in ZnO/rGO composites. A moderate amount of ZnO nanorings (NRs) decorated with rGO can significantly improve the light absorption and photo-luminescence emission because of plasmonic resonant absorption and plasmonic nanoantenna radiation, respectively. ZnO NR/rGO composites with a moderate ZnO content of 29.54 wt.% exhibit the optimum photocatalytic activity with a 0.025 min^{-1} apparent rate constant, which is significantly higher than those of pure rGO (0.0085 min^{-1}) and ZnO NRs (0.018 min^{-1}). The improved performance is ascribed to the synergistic effect of enhanced adsorption capacity, plasmonic light absorption, plasmonic nanoantenna radiation, and the prolonged lifetime of photogenerated electron-hole pairs. Our findings not only offer insights into the plasmon enhanced optical and photocatalytic properties of ZnO NR/rGO composites but also suggest the possibility of fabricating ZnO NR/rGO photocatalyst with enhanced performance.

1. Introduction

Nanorings (NRs) with distinct, closed, and one-dimensional (1D) nanostructures have gained considerable attention because of novel optical [1], electric [2], magnetic [3], and microwave absorbing properties [4–6]. All of these features create new possibilities for improving existing applications. NRs are thought to be plasmonic nanoantennas, which can generate strong electromagnetic (EM) field enhancement effects and distinct absorption in the visible to near-infrared (NIR) regions owing to plasmonic multiresonance [7]. Multiresonant plasmonic nanoantennas offer opportunities for broadband sensor devices [8], coherent control, efficient, solar cell upconverters [9], enhanced nonlinear interactions [10], among others. In addition, enhanced absorption means that ring-like nanostructures would exhibit potential as photocatalysts, but this function remains to be confirmed.

Reduced graphene (rGO), a monolayer sp^2 carbon atom and two-dimensional honeycomb lattice structure, has recently attracted considerable research interest owing to high mobility and conductivity [11], high optical transparency [12], mechanical flexibility [13], chemical stability, and high specific surface area. These excellent features endow the material with numerous applications [11–13], such as photovoltaics, super capacitors, fuel cells, and nanofluids. However, as a single photocatalyst, rGO shows extremely weak photocatalytic activity but high adsorption capacity. If rGO is used as a proper substrate to immobilize and support inorganic semiconductor catalysts, the application performances can be significantly improved. The high charge carrier mobility and specific surface area can improve photocatalytic activity because of enhanced separation efficiency of the photogenerated electron-hole pairs and high adsorption capacity, respectively. The different Fermi levels of rGO and inorganic semiconductors generate a strong heterojunction electric field on the interfaces. The interfacial electric field promotes the swift transfer of photogenerated electrons to the surface of rGO and thus prolongs the lifetime of photogenerated electron-hole pairs. Therefore, rGO-based composites should be investigated for their applications in photocatalysis and photoelectrochemistry. Hereinto, the combination of rGO with ZnO

* Corresponding author.
E-mail addresses: 928221565@qq.com (Y. Zhao), llspzjnu@163.com (L. Liu), wuleiwangyou@163.com, wwhtgs@126.com (T. Cui), tonggx@zjnu.cn (G. Tong), tongwu@zjnu.cn (W. Wu).

http://dx.doi.org/10.1016/j.apsusc.2017.03.207
0169-4332/

may yield enhanced performance because of the excellent individual properties of rGO and ZnO. The morphology, crystallization, band gap, content, and particle size of ZnO nanoparticles determine the properties of ZnO/rGO composites [14–16]. The morphologies of ZnO decorated on rGO surface mainly include microsphere [17], nanowires [18], nanosheets [19], nanorods [20], and hollow dumbbells [21]. Preparation and properties of ZnO nanoring (NR)- and nanobowl (NB)-decorated rGO composites have been rarely reported. To date, ZnO NRs and NBs are fabricated through template strategies [22,23], self-assembly methods [24], or thermal evaporation [25]. However, these approaches present limited practical applications because of high cost and complexity of introducing templates or catalysts to vacuum techniques. Thus far, the fabrication of ring and bowl architectures remains challenging for material chemists.

Given the potential applications of new ZnO NR/NB/rGO composites based on photocatalytic promotion, a simple solution-based chemical etching technique was developed for the one-step fabrication of ZnO/rGO composites with tunable ZnO content and morphology. The content- and shape-dependent optical and photocatalytic properties of ZnO/rGO composites were investigated. The mechanism of the related performance enhancement was also analyzed in this work.

2. Experimental

2.1. Materials

All reagents used except rGO sheets were of analytical grade and used as received without further purification.

2.2. Fabrication of composites of ZnO nanoplate (NP)/rGO, ZnO NB/rGO, and ZnO NR/rGO

The ZnO NP/rGO and ZnO NB/rGO composites were prepared via a hydrolysis and chemical etching approach. In a typical experiment, the dispersion of rGO (10 mg) and H_2O (20.8 mL) in the beaker was achieved by ultrasonication for 10 min. Then cetyltrimethyl ammonium bromide (CTAB, 0.2 g) and $Zn(Ac)_2{\cdot}2H_2O$ (0.1098 g) were added to the dispersion and stirred for 1 h. After 29.2 mL of dimethyl sulfoxide (DMSO) being added into the mixture and stirred for 30 min, the solution was heated at 70 °C for 1.5 h in an oven with the beaker sealed with preservative film. The black ZnO NP/rGO composites were obtained by centrifuging, washing several times with absolute ethanol immediately at the end of reaction and drying in a vacuum oven at 60 °C for 2 h. The ZnO NB/rGO composites were vastly collected if further age the reaction solution at room temperature for 4 h. The process for the synthesis of ZnO NR/rGO composites was similar to the fabrication of ZnO NB/rGO, except that the reaction solution was heated in an oil bath. The ZnO mass fraction in ZnO/rGO composites were tuned by introducing rGO with various masses (5 mg for S3, 10 mg for S4, and 20 mg for S5) to the reaction system.

2.3. Characterization

The phase, composition, morphology, and microstructure of the as-prepared samples were studied by X-ray diffraction (XRD, Y2000, CuKα radiation, $a = 0.15418$ nm, $0.05^\circ\ s^{-1}$), energy dispersive X-ray spectrometry (EDX, EX-250, Horiba, Japan), field-emission scanning electron microscope (FE-SEM, Hitachi S-4800, 5 kV), high-resolution transmission electron microscope (HRTEM, JEM-2100F, 200 kV), and the corresponding selected-area electron diffraction (SAED) pattern. Raman spectra were recorded on a Jobin Yvon HR 800 micro-Raman spectrometer at 457.9 nm. Fourier transform infrared spectra (FTIR) were collected using a NEXUS-670 spectrometer in the ranges of 4000–400 cm^{-1} at room temperature. Brunauer–Emmett–Teller (BET) surface areas (S_{BET}) were determined by a multipoint BET method using the adsorption data in a relative pressure (P/P_0) range of 0.05–0.25 obtained on a Quantachrome Autosorb-1 (Quantachrome Instruments).

2.4. Evaluation of optical properties

Room-temperature optical absorption of the samples in powders was recorded on a Cary 7000 universal measurement spectrophotometer (Agilent Technologies) through wavelength within 300–700 nm. The photo-luminescence (PL) emission spectra of the samples were collected at 360–660 nm by using F-7000 fluorescence spectrophotometer (Hitachi Tokyo Japan), with an excitation wavelength of 325 nm.

2.5. Evaluation of photocatalytic properties

The photocatalytic activity of the as-prepared samples was measured by the degradation of RhB dye under UV light. 5 mg of ZnO/rGO photocatalyst was added to 100 mL RhB in a 200 mL beaker with a concentration of 2.0×10^{-5} mol L^{-1}. A 300 W xenon lamp (NBeT, HSX-F/UV 300) was used as light resource and the mixed solution was then exposed to the UV illumination after stirred in the dark for 1 h to reach adsorption-desorption equilibrium. At given time intervals, 4 mL solutions were sampled and removed the samples by centrifugation. The variations in the absorption band (553 nm) in the UV–vis spectra of RhB were recorded using a UV–vis spectrophotometer (TU-1810).

3. Results and discussion

3.1. XRD and EDX analysis

The phase structure of the samples was analyzed by XRD. The XRD patterns of rGO (S0) and ZnO/rGO composites (S1–S5) are shown in Fig. 1a. The rGO sheets exhibit an extremely weak and broadening (002) diffraction peak at 26.1° (JPCDS 41-1487). The low, broadening peak indicates low crystallinity of the rGO. In addition to the (002) peak, several new diffraction peaks appear in ZnO/rGO composites. These peaks well correspond to wurtzite-structured ZnO (JPCDS 36-1451). The (100) peaks of S1, S2, and S4 were weakened with the ZnO shapes varying from NPs to NBs and NRs. The ZnO diffraction peaks for S5, S4, and S3 are enhanced with the decreased rGO mass because of increasing ZnO content. EDS was employed to determine the elemental composition of the ZnO/rGO composites. EDS spectra in Fig. 1b show the presence of Zn, O, and C in all samples, indicating the formation of ZnO/rGO composites. The Pt peak at about 2.07 keV and the Al peak at about 1.48 keV originated from the conductive film on the surface and bottom of the samples, respectively. The Zn/C atomic ratios in ZnO/rGO composites (S1–S5) are 0.0927, 0.0647, 0.0973, 0.0618, and 0.0360, respectively. Based on XRD patterns and EDX spectra, the mass fractions of ZnO in ZnO/rGO composites (S1–S5) were calculated as 38.60%, 30.50%, 39.76%, 29.54%, and 19.63%, respectively (Table 1). The decreased mass fraction for S1, S2, and S4 is owing to the morphology evolution from NPs to NBs and NRs caused by the etching role; the decreased mass fraction from S3 to S5 is related to the increased rGO mass.

3.2. IR and Raman characterization

The surface chemical structure of the as-obtained products was further confirmed by FTIR and Raman spectra (Fig. 2). Fig. 2a shows the FTIR spectra of ZnO NRs, rGO, and ZnO NR/rGO. For ZnO NRs,

Table 1
Synthesis conditions, physical parameters, and apparent rate constants of ZnO NPs, NBs, and NRs.

NO.	Composite	Experiment conditions[a]	Average side length[b] (nm)	R_{Zn}[c] (%)	S_{BET} ($m^2\ g^{-1}$)	E_g[d]	k[e] (min^{-1})
S0	rGO	/	/	0	135.3	/	0.0085
S1	ZnO NP/rGO (10 mg)	70 °C, one-time volume, 1 h/0 h	160 ± 40	38.60	78.6	3.083	0.017
S2	ZnO NB/rGO (10 mg)	70 °C, one-time volume, 1.5 h/4 h	125 ± 25	30.50	88.69	2.756	0.014
S3	ZnO NR/rGO (5 mg)	70 °C, one-time volume, 1.5 h/4 h, oil bath	145 ± 55	39.76	77.1	3.064	0.021
S4	ZnO NR/rGO (10 mg)			29.54	89.2	2.879	0.025
S5	ZnO NR/rGO (20 mg)			19.63	113.4	2.688	0.013
S6	ZnO NRs			100	9.56	3.177	0.018

[a] Described by reaction temperature, solution volume, reaction time and aging time.
[b] Average side length is obtained from SEM image.
[c] Mass fraction of ZnO in ZnO/rGO composites.
[d] The band gap energy (E_g) was calculated from the Tauc's equation.
[e] The apparent rate constants (k/min^{-1}) is calculated by the equation: $ln\ c_0/c_t = kt$.

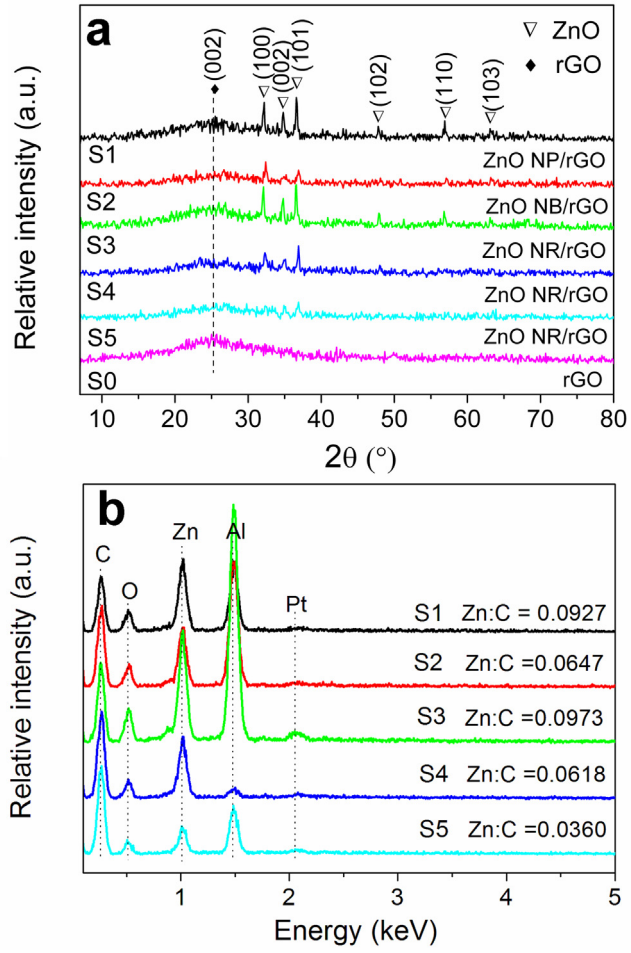

Fig. 1. (a) XRD patterns and (b) EDX spectra of rGO, ZnO, and ZnO/rGO composites.

the strong bands at 3455 cm^{-1} and 1403 cm^{-1} correspond to the surface-absorbed water; bands at 1630 cm^{-1} and 3129 cm^{-1} are related to $-CH_2$ stretching vibrations [26] and $-CH_3$ bending vibrations [27], respectively, caused by the surface absorption of CTAB. The strong and sharp peak at 457 cm^{-1} corresponding to the Zn—O stretching mode is the characteristic absorption of ZnO. For rGO, the weak peaks at 1630 cm^{-1} and 1067 cm^{-1} are assigned to stretching vibration of C=C and C—O, respectively. This indicates the existence of the oxygen-containing functional groups on the surface of rGO sheets. When ZnO NRs was hybridized with rGO sheets, a new absorption band at 1576 cm^{-1} appears in the ZnO NR/rGO composites, which is attributed to the skeletal vibration of the graphene sheets [28].

The Raman spectra in Fig. 2b further confirmed the formation of ZnO NR/rGO composites. For ZnO NRs, the peak at 440 cm^{-1} originates from the nonpolar E_2 vibrational mode and the peak at 582 cm^{-1} is assigned as A1 (LO). The two peaks are the characteristic bands and first-order optical modes of the wurtzite ZnO [29,30]. The band at 677 cm^{-1} corresponds to the A1 mode, which is related to the bond C—C vibration in the CTAB adsorbed on the surface of ZnO. The broad, intense peak at 1150 cm^{-1} is attributed to the TO + LO mode [31]. Both rGO and ZnO NR/rGO show two identical bands but different intensities. The D band at 1346 cm^{-1} is caused by lattice disorders in the sp^2-hybridized C atoms and/or amorphous C deposits; the G band at 1574 cm^{-1} is related to the highly oriented sp^2 hexagonal graphitic lattice [32]. The intensity of I_D/I_G is slightly decreased from 0.81 for rGO to 0.77 for ZnO NR/rGO. The decrease generally is ascribed to the restoration of numerous graphitic domains from amorphous regions of GO [33] and can be explained by the interaction between ZnO NRs and rGO sheets in this study. Additionally, we found that the ZnO growth on rGO induced large enhancement of the Raman signal of rGO at the G and 2D peaks. The Raman enhancement in the G and 2D peaks is generally ascribed to the localized surface plasmon resonance (LSPR). Similar phenomena are also reported in other graphene-based hybrid materials [34].

Raman spectroscopy is a powerful tool to characterize grapheme, which can identify the number of layers [35], the electronic structure [36], the edge structure [37], the type of doping, and any defects [38], in the graphene. In this study, Raman signal is found to strongly depend on the ZnO shape and content in ZnO/rGO composites. Fig. 2c shows the intensity ratio of ZnO/rGO composite to rGO (I_s/I_{s0}) at G and 2D peaks. The I_s/I_{s0} value increases with ZnO shape: I_{s1}/I_{s0}(NPs) < I_{s2}/I_{s0}(NBs) < I_{s4}/I_{s0}(NRs), indicating that bowl-like and ring-like structures are beneficial for LSPR. The I_s/I_{s0} value increases with increasing ZnO content: 19.63% (S5) < 29.54% (S4) < 39.76% (S3), meaning that the high ZnO NR content favors the enhancement of LSPR. Our data demonstrate that the combination of graphene with ZnO plasmonics (bowl and ring) is beneficial for enhancing the optical properties of graphene.

3.3. SEM, TEM, and SAED analysis

Fig. 3a and b shows the SEM images of the typical ZnO NR/rGO composites. The rGO sheets were the curled, corrugated, stromatolithic sheets with 10–25 μm length and 4–7 μm thickness. Numerous ZnO NRs with side lengths of 90–200 nm, height of 80–200 nm, and wall thickness of 30–60 nm were anchored on the surface of rGO sheets (Fig. 3b and c). The intimate contact between ZnO and graphene favors electronic interactions between them and enhanced material charge separation and photocatalytic activity. No periodical lattice stripes were observed in the HRTEM image of rGO sheets (Fig. 3d), confirming that the rGO sheets possess

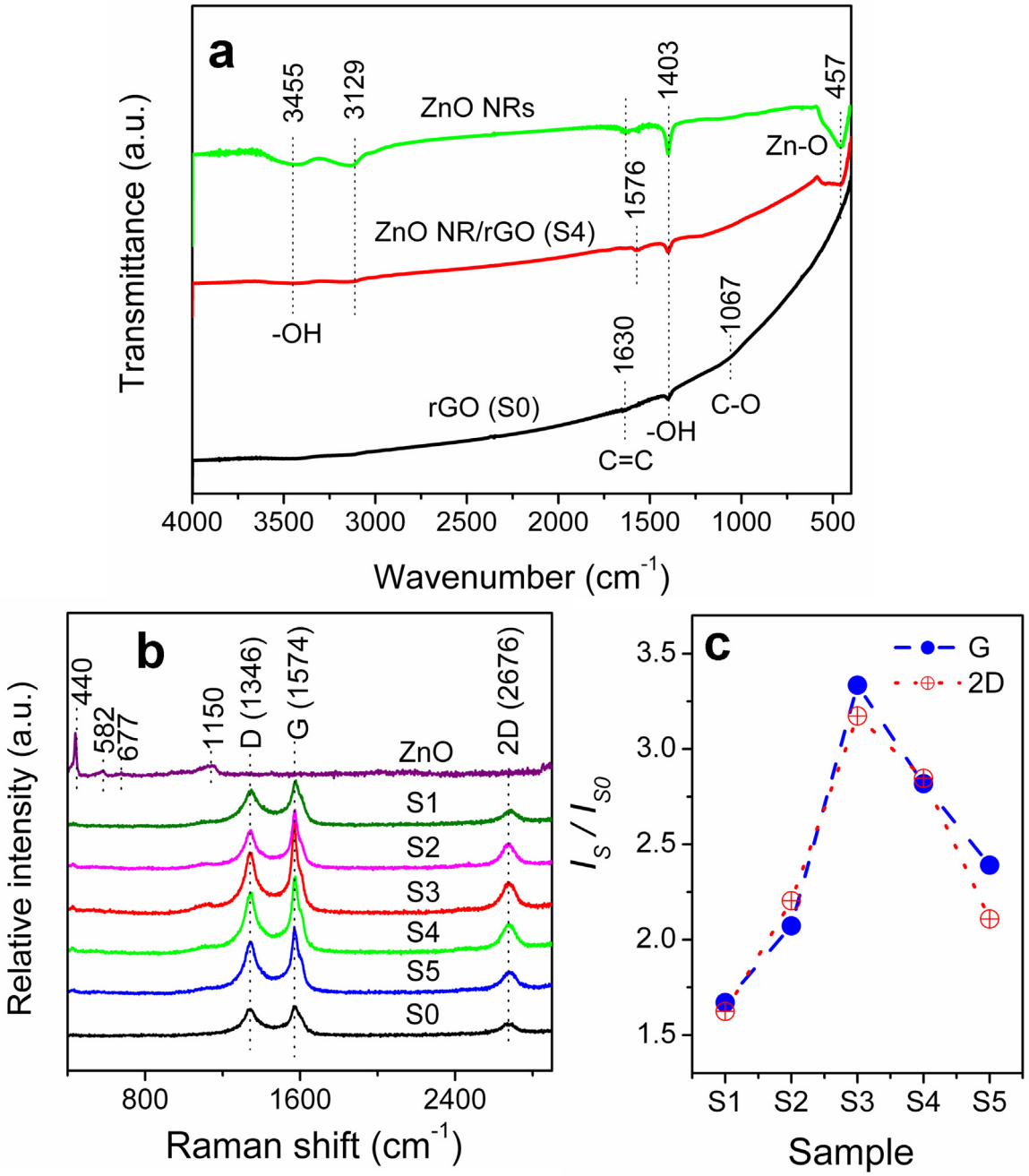

Fig. 2. (a) IR spectra, (b) Raman spectra of rGO, ZnO, and ZnO/rGO composites. (c) The corresponding intensity ratio of ZnO/rGO composite to rGO (I_s/I_{s0}) at G and 2D peaks.

low crystallinity. A TEM image (Fig. 3e) recorded at high magnification clearly showed the perfect hexagonal shape of a complete ring, with typical side length of about 140 nm and wall thickness of 36 nm. Two adjacent side angles of a regular hexagon are 120°. The corresponding SAED pattern (Fig. 3f) indicates that the NR is a single-crystal entity and consist of six side faces [(10–10), (1–100), (0–110), (−1010), (−1100), and (01–10)] with top/bottom surfaces ± (0001). The distributions of C, O, and Zn were clearly resolved by EDX elemental mapping (Fig. 3g–i) and the corresponding bright-field scanning transmission electron microscopy (bright-field STEM) images (Fig. 3j). All these data demonstrate that ZnO NRs are uniformly decorated in the rGO sheets.

For modulating the composition of ZnO NR/rGO composites, rGO sheets with various masses (20, 10, and 5 mg) were introduced to the reaction system. Evidently, the number of ZnO NRs gradually increased with the rGO mass varying from 20 mg to 10 and 5 mg (Figs. 4a–b, 3a–b, and 4c–d). ZnO shape can further be modulated by changing the aging time and heating mode. ZnO NP/rGO composites were obtained by heating the mixture at 70 °C for 1.5 h in an oven without aging. SEM and TEM observations reveal that ZnO decorated on the surface of rGO sheets are single-layer hexagonal NPs (Fig. 4e–g). The side length and thickness are 120–200 and 105–140 nm, respectively. The regular, strong, and clear diffraction spots in the SAED pattern (Fig. 4h) demonstrate the single-crystal nature of NPs. The SAED data demonstrate that the upper and lower end faces of the NPs correspond to the ±(0001) polar surfaces, and the lateral planes consist of non-polar surfaces [±(01–10), ±(10–10), ±(1–100)]. Further aging the above mixture can generate ZnO NB/rGO composites. ZnO is constructed of regularly hexagonal NBs with side lengths of 100–150 nm and thickness of 50–110 nm

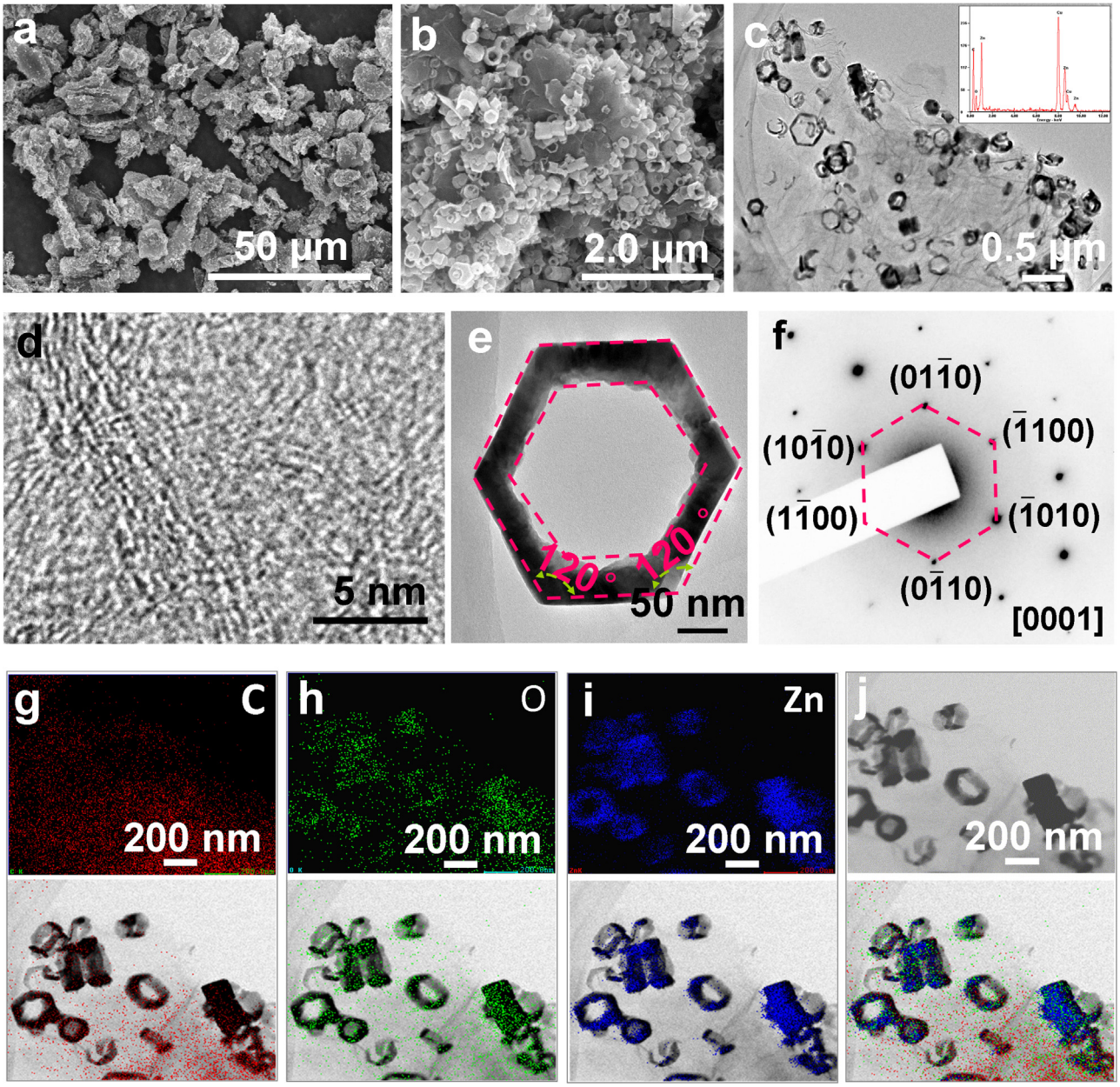

Fig. 3. (a, b) SEM images, (c) TEM image, (d) HR-TEM image, and (g–i) EDX mapping images of the typical ZnO NR/rGO composites. (j) Bright-field STEM images of the corresponding ZnO NR/rGO composites shown in g–i.

(Fig. 4i and k). Various contrasts with light core and dark edge in the TEM image (Fig. 4k) confirm the formation of NBs. SAED analyses (Fig. 4l) confirm the single-crystal nature of ZnO NBs.

3.4. Formation mechanism

The Zn polar surface-guided chemical etching mechanism is proposed for ZnO morphology evolution from NPs to NBs and NRs in ZnO/rGO composites (Fig. 5). The chemical reactions in the reaction system are as follows.

$$Zn(CH_3COO)_2 + 2H_2O \underset{\longleftarrow}{\rightarrow} Zn(OH)_2 + 2CH_3COOH \quad (1)$$

$$Zn(OH)_2 \underset{\longleftarrow}{\rightarrow} ZnO + H_2O \quad (2)$$

$$DMSO + H_2O \underset{\longleftarrow}{\rightarrow} [DMSO - H]^+ + OH^- \quad (3)$$

$$Zn^{2+} + 4OH^- \underset{\longleftarrow}{\rightarrow} [Zn(OH)_4]^{2-} \quad (4)$$

In the DMSO-H_2O system, spontaneously hydrolyzation of $Zn(CH_3COO)_2$ forms $Zn(OH)_2$ precipitates (Reaction (1)) on the surface of rGO, which subsequently are transformed into ZnO nuclei (Reaction (2)). DMSO functions not only as solvent but also as a reactant to provide OH^- ions through hydrolysis in the solution (Reaction (3)). A mass of DMSO polar molecules absorbed on the (0001)-Zn polar faces stunt the ZnO growth along the [0001] direction, resulting in the formation of hexagonal ZnO NPs. DMSO polar molecules release numerous OH— ions. Owing to the electrostatic interaction, OH— ions are preferentially adsorbed on the positive (0001)-Zn polar plane of ZnO hexagonal NPs, leading to fast etching along the – [0001] direction (Reaction 4). Prolonging the aging time

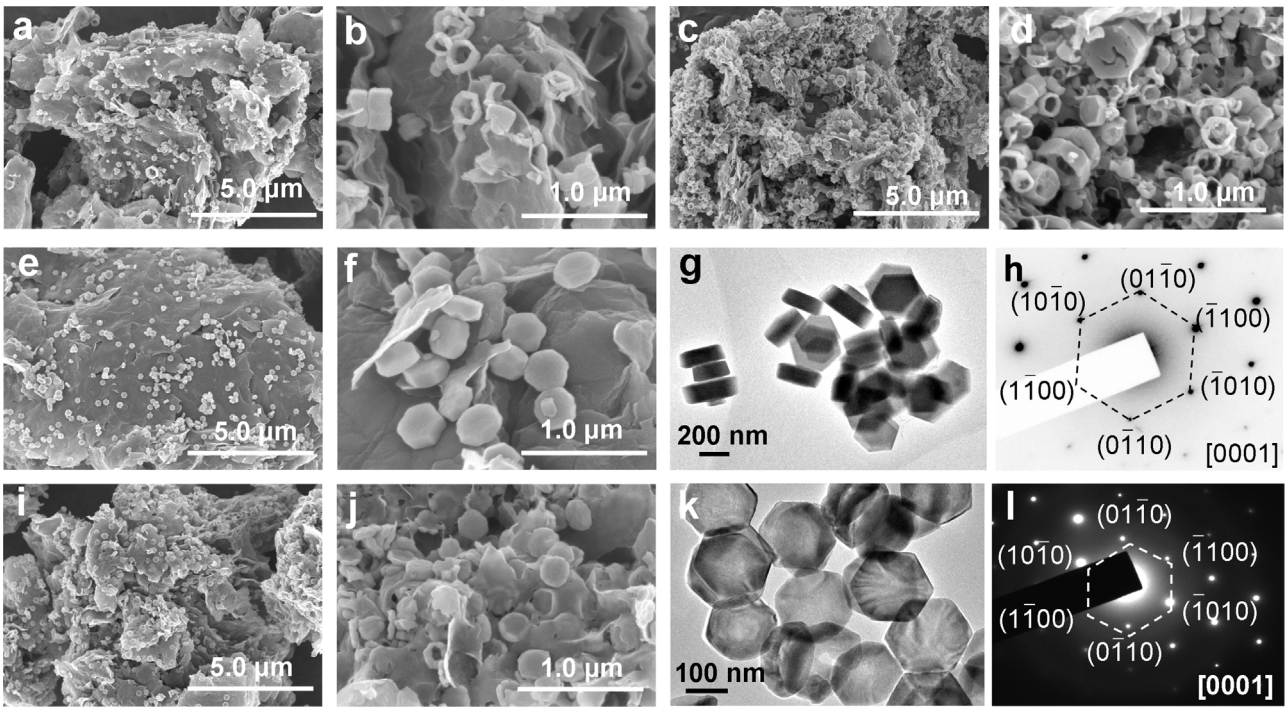

Fig. 4. (a–d, e–f, and i–j) SEM images, (g and k) TEM images, and (h and l) SAED patterns of (a–d) ZnO NR/rGO composites, (e–h) ZnO NP/rGO composites, and (i–l) ZnO NB/rGO composites.

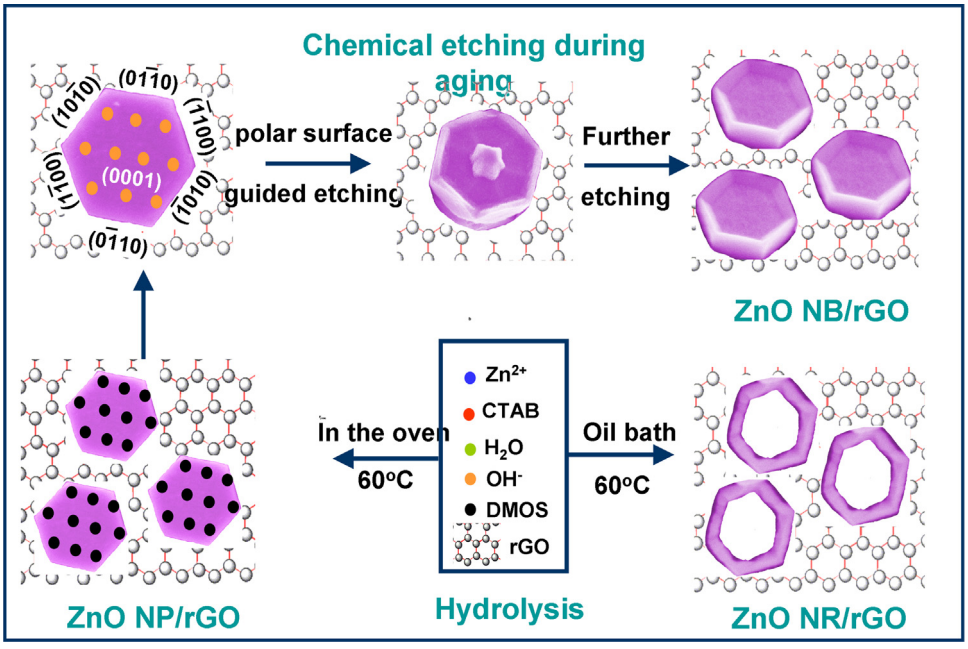

Fig. 5. Schematic of the formation mechanism of ZnO/rGO composites.

favors the morphological evolution from ZnO NPs to ZnO mushrooms and bowls (see Fig. S1a–S1c). We found that the ZnO NBs and NRs can form at just low aging temperatures because a slow reaction generates different growth and etching rates in different crystal faces, forming the anisotropic structures. Structurally, ZnO contains three rapid growth directions: ⟨2-1-10⟩ (±[2-1-10], ±[-12-10], ±[-1-120]); <01–10> (±[01-10], ±[10–10], ±[1–100]); and ± [0001] [39]. The surface energy of the two polar planes [±(0001)] is higher than that of the nonpolar planes [{2-1-10}, and {01–10}]. The etching growth tends to maximize the areas of the {2-1-10} and {01–10} facets, thus following the principle of low surface free energy. Further extension of aging time induces the formation of ring-like structures (Fig. S1d). Ring-like structures are also formed in an oil bath (Fig. 5). In addition, CTAB plays a key role in the formation of NBs and NRs. In the absence of CTAB, the etching reaction will preferentially occur on the edge of NPs, resulting in the formation of just mushroom-shape ZnO NPs (Fig. S2a). In the presence of CTAB, the steric exclusion from CTAB adsorption on the surface of NPs will depress the etching role of OH^- ions, leading to the formation of ZnO NBs (Fig. S2b). Further increasing CTAB mass favors the NR formation (Fig. S2c).

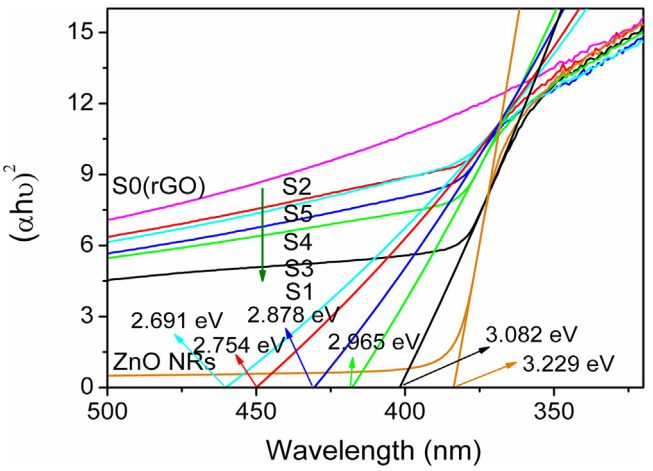

Fig. 6. Band gap energy (Eg) versus ZnO shape and content of ZnO/rGO composites (S1–S5) obtained from the UV-absorption spectra.

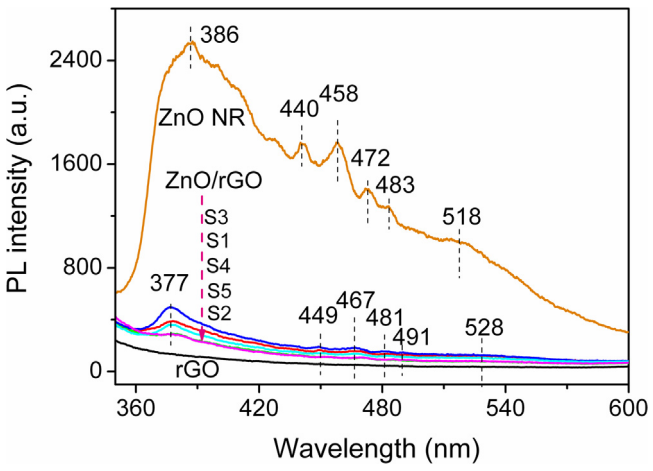

Fig. 7. Room temperature PL spectra from ZnO NRs, rGO (S0), and ZnO/rGO composites (S1–S5).

3.5. UV-absorption characteristics

Fig. 6 shows the UV-absorption characteristics of ZnO/rGO composites. A fundamental absorption sharp edge rising at 380 nm is the characteristic spectrum of pure ZnO NRs. A strong absorption background in the whole visible and UV regions is observed for pure rGO that is consistent with that of reported graphene sheets [14]. The strong absorption was related to the excitation of broadened surface plasmonic modes in graphene and the breakdown of the Dirac-fermion model caused by triangular warping and nonlinearity of energy bands far from the Dirac energy [40,41]. Owing to the presence of rGO with zero band gap, the wavelength response range of ZnO/rGO composites was expanded to the visible region with similar absorption band-edges to ZnO. In general, the rate of the photocatalytic reaction is proportional to $[(I_\alpha\phi)^n$ ($n = 1$ for low light intensity, $n = 1/2$ for high light intensity)], where I_α is the photon-numbers absorbed by photocatalyst per second and &x3D5; is the efficiency of the band gap transition [42]. Enhanced photoreactivity can be partly explained by the intensive absorbance in the UV region, resulting in an increase in I_α. In our studies, the absorption intensity varies in the order of rGO > S2 > S5 > S4 > S3 > S1 > ZnO in the range of 380–500 nm. This change is related to the mass fraction and shape of ZnO loading. A comparison of S3–S5 reveals that higher ZnO NRs content translates to lower absorption intensity. The change trend is opposite to that of reported rGO/ZnO nanohybrids [33]. However, the higher ZnO content and larger I_α of S3 than S1 indicates that NRs possess higher absorbance than NPs; the higher ZnO content and larger I_α of S2 than S4 means that the absorbance of NBs is larger than that of NRs. Enhanced absorption effect was found in ZnO NBs [43] and Co_3O_4 nano/microlotus leaves [44] because of the light concentration and gain effects, respectively. Owing to the presence of the positively charged (001) Zn-polar and negatively charged (001) O-polar surfaces, a normal dipole moment and spontaneous polarization will occur along the *c* axis of ZnO NRs [45–48]. Under an alternating electromagnetic (EM) field, the photogenerated electrons from the polar planes or oxygen vacancies migrate to form relaxation polarization. In this case, as a simple plasmonic structure, ZnO NRs exhibit surface plasmon resonant absorption because of the coupling of dipolar modes on the inner and outer surfaces of the NRs.

The absorption edge shifts indicate the changes in the band gap energy (E_g) of ZnO/rGO composites. The optical band gap of crystalline semiconductors can be calculated from Tauc's equation [49]: $\alpha h\nu = A(h\nu\text{-}E_g)^n$, in which E_g is the optical band gap, α is the absorption coefficient, h is Planck's constant, ν is the frequency of light, A is a constant for the material, and n is 2 for ZnO (direct transition mode materials). The value of E_g can be obtained by extrapolating the linear region of a plot of $(\alpha h\nu)^2$ on the y-axis versus photon energy ($h\nu$) on the x-axis. Fig. 6 shows the E_g values of ZnO/rGO composites with different shapes and contents of ZnO loading. The E_g was 3.082 eV for ZnO NP/rGO composites (S1), 2.754 eV for ZnO NB/rGO composites (S2), and 2.878 eV for ZnO NR/rGO composites (S4) (Fig. 6). The E_g for ZnO NR/rGO composites (S3–S4) gradually decreases with decreasing ZnO content. A similar phenomenon was found in semiconductor-rGO nanocomposites and could be ascribed to synergistic interfacial interaction between the semiconductor and rGO [50]. All of the broadened wavelength response range, enhanced light absorption, and low E_g indicate that the combination of rGO sheets with ZnO NRs would enhance photocatalytic activity.

3.6. PL spectrum analysis

Fig. 7 shows the photoluminescence (PL) emission (excited at 325 nm) spectra of the samples. No significant emitting bands can be observed in pure rGO, whereas six strong emitting bands appear in pure ZnO NRs. A strong ultraviolet emission peak at 386 nm corresponding to near band-edge emission is attributed to the excitonic recombination of a hole in the valence band and an electron in the conduction band. The weak blue-green emission band at about 460 nm is induced by Xe lamp [51]. Other four weak emitting peaks at 440–518 nm generally originate from the different kinds of defects in ZnO, including oxygen zinc vacancy (V_{Zn}) or interstitial oxygen (O_i) owing to the rich O in the as-obtained ZnO samples [52].

PL originates from the recombination of electron-hole pairs after a photocatalyst is irradiated. Therefore, the intensity of emitting bands can be used to reflect the fate of electron-hole pairs [53]. The strong emitting bands correspond to the high recombination rate of photogenerated electron-hole pairs. Compared with pure ZnO NRs, ZnO/rGO composites exhibit weaker emitting peaks. Graphene is a good electron acceptor [54], and semiconductor ZnO is a good electron donor [55]. Graphene accepted the photogenerated electron, which promoted interfacial electron transfer from the adhered ZnO and thus weakened emitting peaks. Weaker emitting peaks indicate that the composites of rGO and ZnO can effectively retard the recombination rate of photogenerated electron-hole pairs. The intensities of emitting peaks change in the order of $I_{ZnO} > I_{S3} > I_{S1} > I_{S4} > I_{S5} \approx I_{S2} > I_{GO}$. This change may be associated with ZnO content and morphology. A high ZnO content

induced strong emission. When the ZnO content is extremely close, $I_{S3} > I_{S1}$ and $I_{S4} > I_{S5} \approx I_{S2}$ reveal ring-like structure can generate the strong emitting peak. The interesting emission enhancement should be ascribed to ring-like structures, which generate plasmonic electromagnetic field enhancements.

The optical properties are dominated by the excitation of collective oscillations of ZnO NR conduction band electrons. When an electromagnetic wave falls on a NR, the photogenerated electrons are excited by axial, radial, and azimuthal polarizations when a suitable spectral band is selected [1]. The excited electrons oscillate collectively as a wave (plasmon) [56]. In this study, the ZnO NR can act as a plasmonic nanoantenna, which emits either a confined magnetic field or a confined electric field, resulting in an electromagnetic field enhancement. The energy of nanoantenna radiation depends on particle size, shape, composition, interparticle spacing, and dielectric environment [57,58]. Similar plasmon EM field enhancement has been found in Au NRs [58,59]. These plasmonic nanoantennas exhibit surface-enhanced Raman scattering spectroscopy [60], surface-enhanced infrared spectroscopy [61], antenna-enhanced ultrafast nonlinear spectroscopy [62], and near-field microscopy [63], and others. Meanwhile, a slight change in the position of emission peaks occurred. A blue shift was found in the UV emitting band at 386 nm, and a red shift was observed for emitting bands at 440–518 nm. The former may be related to a strong heterojunction electric field generated on the interface of graphene and ZnO owing to the difference in Fermi levels. The heterojunction electric field promotes the separation of photogenerated electrons and holes but impedes their recombination, resulting in the blue shift. The latter may be due to the introduction of new defect sites (or recombination centers) caused by rGO. In a word, our PL measurement results confirm that the compound of rGO and ZnO can effectively suppress recombination of photogenerated electrons and holes.

3.7. Photocatalytic properties

Rhodamine B (RhB) solution was selected as a typical pollutant to investigate the influence of ZnO morphology and content on the photocatalytic activities of the ZnO/rGO composites. Fig. 8a and b show the UV–vis absorption spectra of an RhB aqueous solution containing 5 mg ZnO/rGO powders after exposure to UV for different durations. The peak intensity was rapidly decreased with the extension of irradiation time, accompanied by a slight shift to shorter wavelengths. No new absorption bands appear in either the visible or ultraviolet regions, indicating the complete photodegradation of RhB. After 1 h of adsorption-desorption in the dark, the main absorption peak at 553 nm corresponding to the RhB molecules decreases by only 2% for pure ZnO NRs, approximately 10% for ZnO NR/rGO, and 21% for rGO (Fig. 8c and d). This result indicates that a compound of rGO and ZnO can evidently improve the adsorption capacity of single-crystal ZnO nanostructures.

The blank experiment shows that only a slow decrease in RhB concentration was detected under UV irradiation (Fig. 8c) in the absence of a catalyst. After 140 min of UV irradiation, only 70% pho-

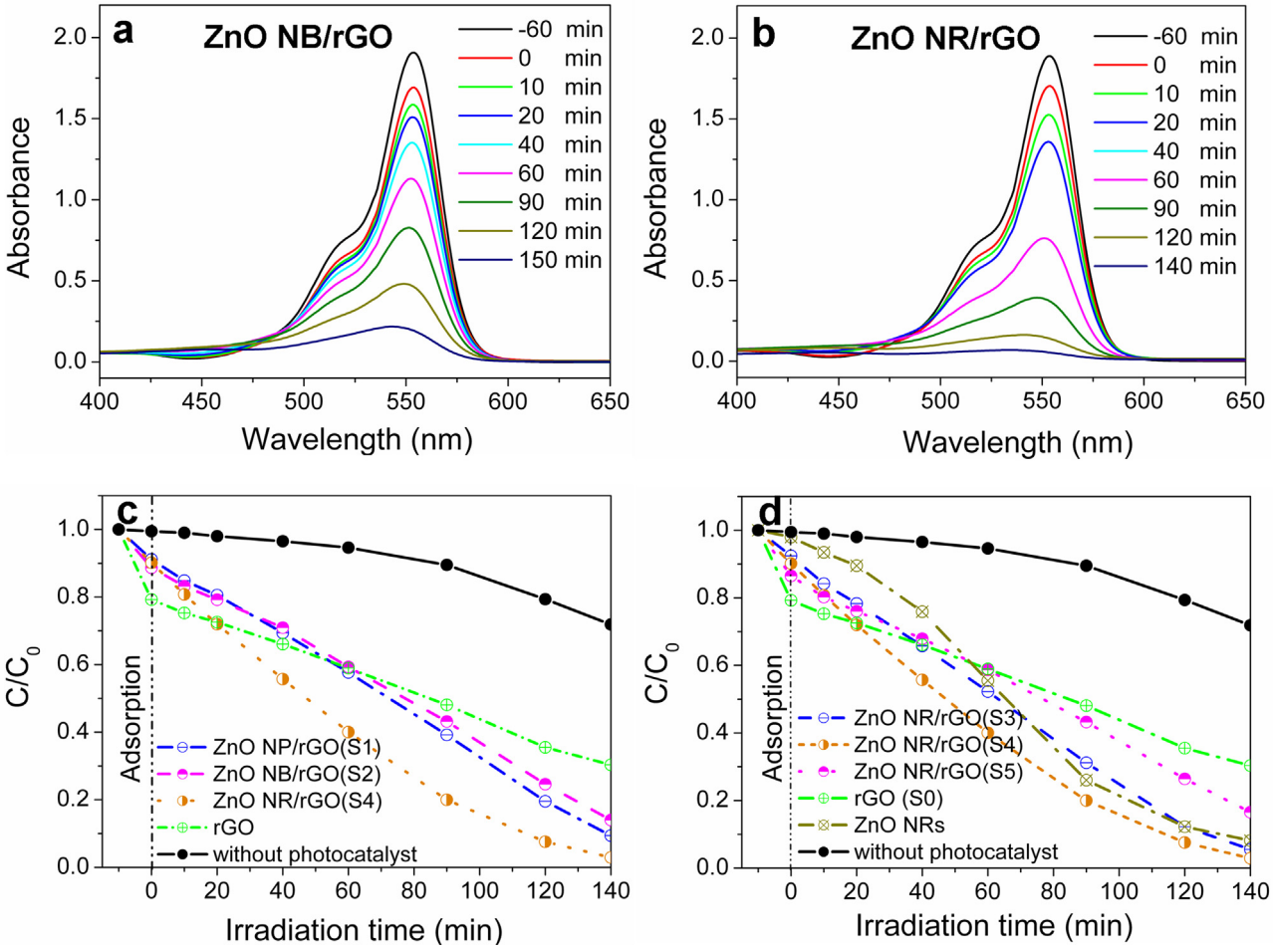

Fig. 8. Photocatalytic degradation of RhB on ZnO/rGO composites under UV–vis light illumination. (a–b) UV–vis spectral changes in RhB aqueous solutions as a function of irradiation time in the presence of ZnO NB/rGO and ZnO NR/rGO composites. Change in RhB normalization concentration (from the optical absorbance measurements at 553 nm) over ZnO/rGO composites with various ZnO shapes (c) and various ZnO contents (d) as a function of irradiation time.

Table 2
Summary of photocatalytic properties for ZnO and its composites.

Sample	RhB concentration ($mol\,L^{-1}$)	catalyst concentration ($g\,L^{-1}$)	discoloration rate (%) and time (min)	Reference
ZnO nanospheres-1% rGO	2.09×10^{-5}	0.25	68/120	[44]
ZnO nanospheres-5% rGO			88/120	
ZnO nanospheres-10% rGO			93/120	
ZnO nanospheres-30% rGO			75/120	
plate-like ZnO	1.25×10^{-5}	1.0	94/180	[59]
hollow ZnO nanospheres	2.1×10^{-5}	0.6	100/150	[62]
ZnO nanodisks	1.25×10^{-5}	1	98.5/500	[63]
rGO	2.0×10^{-5}	0.05	70/140	This
ZnO NP/rGO			91/140	work
ZnO NB/rGO			86/140	
ZnO NR/rGO			92/120, 97/140	

todegradation of RhB occurred for pure rGO and 92% for pure ZnO NRs. When rGO was decorated by a small quantity of ZnO NRs (that is, Zn content = 29.54 wt.%), ZnO NR/rGO composites exhibit the highest photocatalytic activities with 97% discoloration in 140 min. The photocatalytic activities of ZnO NR/rGO composites are higher than those of pure ZnO NRs, ZnO nanostructures with other morphologies (Table 2). To reveal the enhancement mechanism of ZnO NR/rGO composites, we systematically investigated the influences of ZnO shape and content on the photocatalytic activity of the ZnO/rGO composites. Seen from Fig. 8c, ZnO content-dependent photocatalytic activities of ZnO NR/rGO composites follow the order of k19.63 < k39.76 < k29.54. Evidently, rGO decorated by an appropriate amount of ZnO NRs can significantly improve photocatalytic activity. Fig. 8d shows 90% discoloration for ZnO NP/rGO, 86% discoloration for ZnO NB/rGO, and 97% discoloration for ZnO NR/rGO. The ZnO morphology-dependent photocatalytic activities of ZnO/rGO composites vary in the order of NBs < NPs < NRs.

The photocatalytic mechanism has been proposed for ZnO NR/rGO composites based on the above results (Fig. 9). Upon UV irradiation, the electron–hole (e^-–h^+) pairs generate between conduction (CB) and valence bands (VB) of ZnO. The photogenerated e^- and h+ react with O_2 and OH^-, respectively, to form super oxide anion $^{\bullet}O_2^-$ and $^{\bullet}OH$. The free radicals (i.e., $^{\bullet}OH$, $^{\bullet}O_2^-$, $HOO^{\bullet}$) further react with RhB molecules on the surface of ZnO and degrade them to non-toxic products [16,17,48]. The enhanced photocatalytic activities should be ascribed to the following several aspects. First, a compound of rGO with high S_{BET} ($135.3\,m^2\,g^{-1}$) and ZnO with low S_{BET} ($9.56\,m^2\,g^{-1}$) can improve the specific surface area (Table 1). A high S_{BET} can adsorb more RhB molecules and facilitate the harvesting of exciting light (confirmed by UV absorption spectra in Fig. 6), thereby accelerating the photocatalytic reaction. As the ZnO content in ZnO/rGO composites decreases, the S_{BET} of ZnO/rGO composites gradually increases (Table 1); the interface surface between rGO and ZnO and the surface active sites for the adsorption of RhB molecules on ZnO photocatalyst surfaces decrease. The former will improve the adsorption of RhB molecules and the latter will slow down the photocatalytic reaction. In this case, ZnO NR/rGO composites reach the optimal photocatalytic activity with

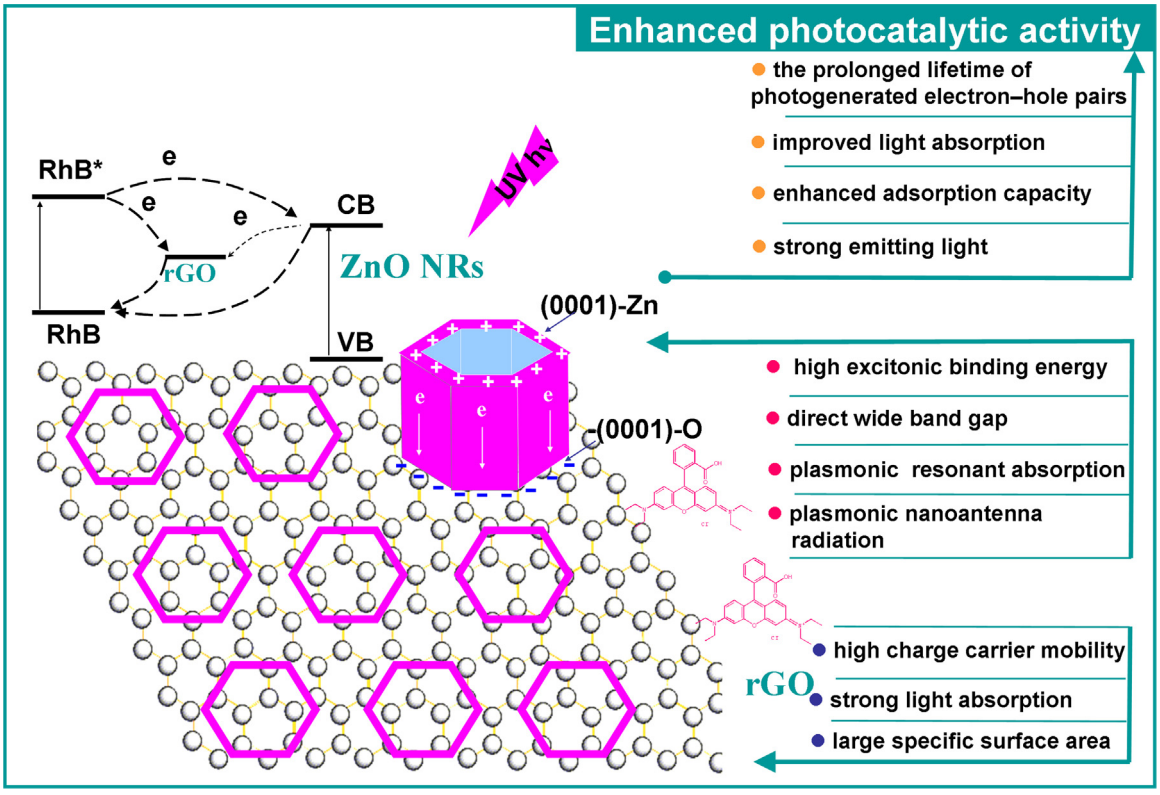

Fig. 9. Mechanical illustration of enhanced photocatalytic activity for rGO/ZnO NR composites.

a 0.025 min^{-1} apparent rate constant at a moderate ZnO content of 29.54 wt.%.

Second, the Fermi level of graphene (0 V vs NHE) is less negative than the conduction band of ZnO. The difference in Fermi levels generates a strong heterojunction electric field on the interface between graphene and ZnO. Photogenerated electrons are swiftly transferred from ZnO to the surface of graphene, thus prolonging the lifetime of photogenerated electron–hole pairs and markedly enhancing photocatalytic ability. Meanwhile, rGO generally functions as an electron sink in the photocatalytic system and its high charge carrier mobility can promote the separation efficiency of the photogenerated electron-hole pairs[64] and enhance photocatalytic activity. Moreover, ZnO NRs with hollow structure facilitates the transportation of photogenerated electron from ZnO to rGO. Third, the combination of graphene with ZnO nanoparticles decreases the band gap energy (E_g) (Table 1). The small E_g can improve photocatalytic properties because of the effective absorption of exciting light in the larger range [65]. Seen from Table 1, ZnO NR/rGO composites exhibit larger E_g value and higher photocatalytic activity than those of ZnO NB/rGO composites. This indicates that the ring-like configuration contributes greatly to the enhanced activity. Fourth, the unique morphology performs a key function in the enhanced photocatalytic activities. Compared with ZnO NBs and NPs, ZnO NRs can provide more surface active sites for the adsorption of pollutant molecules and facilitate the harvesting of exciting light by plasmonic resonant absorption and the transportation of photogenerated electron and pollutant molecules within the hole, resulting in enhanced intensity of absorption in the UV–vis light region [66,67]. Besides, stronger emitting light caused by plasmonic nanoantenna radiation will work as the second light source and induce higher photocatalytic activity. The Raman data in Fig. 2c confirm that ZnO NR/rGO composites exhibit stronger LSPRs than those of ZnO NP/rGO and ZnO NB/rGO composites due to the distinct geometric configuration of NRs. The NRs are plasmonic structures with distinct polarization and coupling modes on the inner and outer surfaces of the NRs, which enhance electromagnetic field and distinguishable plasmonic resonance absorption. In brief, the enhancement of photocatalytic activity exhibited by ZnO NR/rGO can be ascribed to the integrative synergistic effect of improved adsorption capacity, plasmonic light absorption, plasmonic nanoantenna radiation, and the prolonged lifetime of photogenerated electron-hole pairs.

4. Conclusions

A series of ZnO/rGO composites were prepared through an easy low-temperature chemical etching route. The ZnO shape and content in ZnO/rGO composites can be adjusted by changing aging time, heating mode, and mass of rGO added. The influences of ZnO shape and content on optical and photocatalytic properties of ZnO/rGO composites are investigated in depth. ZnO NBs and NRs with low contents favor the light absorption of ZnO/rGO composites because of light concentration, plasmon resonant absorption, and the higher absorption of rGO than ZnO; ZnO NR/rGO composites exhibit stronger PL emission spectra in comparison with those of ZnO NP/rGO and ZnO NB/rGO composites because of plasmonic nanoantenna radiation. The optimum photocatalytic activity with an apparent rate constant of 0.025 min^{-1} is exhibited by ZnO NR/rGO composites with a moderate ZnO content of 29.53 wt.%, which is significantly higher than those of pure rGO (0.0085 min^{-1}) and ZnO NRs (0.018 min^{-1}). Improved performance is ascribed to the synergistic effect of plasmonic light absorption, plasmonic nanoantenna radiation, enhanced adsorption capacity, and the prolonged lifetime of photogenerated electron-hole pairs. Owing to enhanced optical and photocatalytic activity, ZnO NR/rGO composites are promising for practical use in pollutant decomposition as effective photocatalysts.

Acknowledgements

This project was financially supported by the National Natural Science Foundation of China (51672252 and 51102215), Public Utility Items of Zhejiang Province (2015C31022), and Natural Scientific Foundation of Zhejiang Province (LY14B010001).

Appendix A. Supplementary data

Supplementary data associated with this article can be found, in the online version, at http://dx.doi.org/10.1016/j.apsusc.2017.03.207.

References

[1] M.A. Suarez, T. Grosjean, D. Charraut, D. Courjon, Nanoring as a magnetic or electric field sensitive nano-antenna for near-field optics applications, Opt. Commun. 270 (2007) 447–454.
[2] A.V. Maslov, D.S. Citrin, Enhancement of the Aharonov-Bohm effect of neutral excitons in semiconductor nanorings with an electric field, Phys. Rev. B 67 (2003) 121304.
[3] Y.G. Yoo, M. Kläui, C.A.F. Vaz, L.J. Heyderman, J.A.C. Bland, Switching field phase diagram of Co nanoring magnets, Appl. Phys. Lett. 82 (2003) 2470–2472.
[4] Y. Liu, T.T. Cui, T. Wu, Y.N. Li, G.X. Tong, Excellent microwave absorbing properties of elliptical Fe_3O_4 nanorings made by a rapid microwave-assisted hydrothermal approach, Nanotechonolgy 27 (2016) 165707.
[5] G.X. Tong, Y. Liu, T.T. Cui, Y.N. Li, Y.T. Zhao, J.G. Guan, Tunable dielectric properties and excellent microwave absorbing properties of elliptical Fe_3O_4 nanorings, Appl. Phys. Lett. 108 (2016) 072905.
[6] T. Wu, Y. Liu, X. Zeng, T.T. Cui, Y.T. Zhao, Y.N. Li, G.X. Tong, Facile hydrothermal synthesis of Fe_3O_4/C core-shell nanorings for efficient low-frequency microwave absorption, ACS Appl. Mater. Inter. 8 (2016) 7370–7380.
[7] R. Alaee, D. Lehr, R. Filter, F. Lederer, E.B. Kley, C. Rocktuhl, A. Tünnermann, Scattering dark states in multiresonant concentric plasmonic nanorings, ACS Photonics 2 (2015) 1085–1090.
[8] K. Aydin, V.E. Ferry, R.M. Briggs, H.A. Atwater, Broadband polarization-independent resonant light absorption using ultrathin plasmonic super absorbers, Nat. Commun. 2 (2011) 517.
[9] H.A. Atwater, A. Polman, Plasmonics for improved photovoltaic devices, Nat. Mater. 9 (2010) 205–213.
[10] W.S. Cai, A.P. Vasudev, M.L. Brongersma, Electrically controlled nonlinear generation of light with plasmonics, Science 333 (2011) 1720–1723.
[11] K.I. Bolotin, K.J. Sikes, Z. Jiang, M. Klima, G. Fudenberg, J. Hone, P. Kim, H.L. Stormer, Ultrahigh electron mobility in suspended grapheme, Solid State Commun. 146 (2008) 351–355.
[12] X.S. Li, Y.W. Zhu, W.W. Cai, M. Borysiak, B.Y. Han, D. Chen, R.D. Piner, D.P. Luigi, Transfer of large-area graphene films for high-performance transparent conductive electrodes, Nano Lett. 9 (2009) 4359–4363.
[13] C. Lee, X.D. Wei, J.W. Kysar, J. Hone, Measurement of the elastic properties and intrinsic strength of monolayer grapheme, Science 321 (2008) 385–388.
[14] T.G. Xu, L.W. Zhang, H.Y. Cheng, Y.F. Zhu, Significantly enhanced photocatalytic performance of ZnO via graphene hybridization and the mechanism study, Appl. Catal. B 101 (2011) 382–387.
[15] Y.Y. Bu, Z.Y. Chen, W.B. Li, B.R. Hou, Highly efficient photocatalytic performance of graphene-ZnO quasi-shell-core composite material, ACS Appl. Mater. Inter. 5 (2013) 12361–12368.
[16] R. Beura, P. Thangadurai, Structural, optical and photocatalytic properties of graphene-ZnO nanocomposites for varied compositions, J. Phys. Chem. Solids 102 (2017) 168–177.
[17] J.Q. Qin, X.Y. Zhang, C.W. Yang, M. Cao, M. Ma, R.P. Liu, ZnO microspheres-reduced graphene oxide nanocomposite for photocatalytic degradation of methylene blue dye, Appl. Surf. Sci. 392 (2017) 196–203.
[18] X.W. Fu, Z.M. Liao, Y.B. Zhou, H.C. Wu, Y.Q. Bie, J. Xu, D.P. Yu, Graphene/ZnO nanowire/graphene vertical structure based fast-response ultraviolet photodetector, Appl. Phys. Lett. 100 (2012) 223114.
[19] X.J. Liu, L.K. Pan, T. Lv, T. Lu, G. Zhu, Z. Sun, C.Q. Sun, Microwave-assisted synthesis of ZnO-graphene composite for photocatalytic reduction of Cr[VI], Catal. Sci. Technol. 1 (2011) 1189–1193.
[20] E. Rokhsata, O. Akhavan, Improving the photocatalytic activity of graphene oxide/ZnO nanorod films by UV irradiation, Appl. Surf. Sci. 371 (2016) 590–595.
[21] X.L. Yu, G.J. Zhang, H.B. Cao, X.Q. An, Y. Wang, Z.J. Shu, X.L. An, F. Hua, ZnO@ZnS hollow dumbbells-graphene composites as high-performance photocatalysts and alcohol sensors, New J. Chem. 36 (2012) 2593–2598.

[22] Y.F. Wang, X.L. Chen, J.H. Zhang, Z.Q. Sun, Y.F. Li, K. Zhang, B. Yang, Fabrication of surface-patterned and free-standing ZnO nanobowls, Colloids Surf. A 329 (2008) 184–189.
[23] Y.F. Wang, J.H. Zhang, X.L. Chen, X. Li, Z.Q. Sun, K. Zhang, D.Y. Wang, B. Yang, Morphology-controlled fabrication of polygonal ZnO nanobowls templated from spherical polymeric nanowell arrays, J. Colloid Interface Sci. 322 (2008) 327–332.
[24] K.S. Krishna, U. Mansoori, N.R. Selvi, M. Eswaramoorthy, Form emerges from formless entities: temperature-induced self-assembly and growth of ZnO nanoparticles into zeptoliter bowls and troughs, Angew. Chem. Int. Ed. 46 (2007) 5962–5965.
[25] Z.L. Zhang, G. Zheng, F.Y. Qu, X. Wu, ZnO microbowls grown on an ITO glass substrate through thermal evaporation, Chin. Phys. B 21 (2012) 098104.
[26] Y.D. Wang, S. Zhang, C.L. Ma, H.D. Li, Synthesis and room temperature photoluminescence of ZnO/CTAB ordered layered nanocomposite with flake-like architecture, J. Lumin. 126 (2007) 661–664.
[27] O. Mondal, M. Pal, Strong and unusual violet-blue emission in ring shaped ZnO nanocrystals, J. Mater. Chem. 21 (2011) 18354–18358.
[28] W.B. Zou, J.W. Zhu, Y.X. Sun, X. Wang, Depositing ZnO nanoparticles onto graphene in a polyol system, Mater. Chem. Phys. 125 (2011) 617–620.
[29] S. Kumar, P.D. Sahare, Observation of band gap and surface defects of ZnO nanoparticles synthesized via hydrothermal route at different reaction temperature, Opt. Commun. 285 (2012) 5210–5216.
[30] R. Cuscó, E. Alarcón-Lladó, J. Ibánez, L. Artús, J. Jiménez, B. Wang, M.J. Callahan, Temperature dependence of Raman scattering in ZnO, Phys. Rev. B: Condens. Matter Mater. Phys. 75 (2007) 165202.
[31] M. Šćepanović, M. Grujić-Brojčin, K. Vojisavljević, S. Bernik, T. Srećković, Raman study of structural disorder in ZnO nanopowders, J. Raman Spectrosc. 41 (2010) 914–921.
[32] H.G. Fan, X.T. Zhao, J.H. Yang, X.N. Shan, L.L. Yang, Y.J. Zhang, X.Y. Li, M. Gao, ZnO-graphene composite for photocatalytic degradation of methylene blue dye, Catal. Commun. 29 (2012) 29–34.
[33] Y. Liu, Y. Hu, M.J. Zhou, H.S. Qian, X. Hu, Microwave-assisted non-aqueous route to deposit well-dispersed ZnO nanocrystals on reduced graphene oxide sheets with improved photoactivity for the decolorization of dyes under visible light, Appl. Catal. B 125 (2012) 425–431.
[34] W.L. Barnes, A. Dereux, T.W. Ebbesen, Surface plasmon subwavelength optics, Nature 424 (2003) 824–830.
[35] J.S. Park, A. Reina, R. Saito, J. Kong, G. Dresselhau, M.S. Dresselhaus, G′ band Raman spectra of single, double and triple layer grapheme, Carbon 47 (2009) 1303–1310.
[36] L.M. Malard, J. Nilsson, D.C. Elias, J.C. Plentz, E.S. Alves, A.H. Castro Neto, M.A. Pimenta, Probing the electronic structure of bilayer graphene by Raman scattering, Phys. Rev. B 76 (2007) 201401.
[37] Y. You, Z. Ni, T. Yu, Z. Shen, Edge chirality determination of graphene by Raman spectroscopy, Appl. Phys. Lett. 93 (2008) 163112.
[38] H. Liu, S. Ryu, Z. Chen, M.L. Steigerwald, C. Nuckolls, L.E. Brus, Photochemical Reactivity of Graphene, J. Am. Chem. Soc. 131 (2009) 17099–17101.
[39] Z.L. Wang, Zinc oxide nanostructures: growth, properties and applications, J. Phys. Condens. Matter 16 (2004) R829.
[40] R.R. Nair, P. Blake, A.N. Grigorenko, K.S. Novoselov, T.J. Booth, T. Stauber, N.M.R. Peres, A.K. Geim, Fine structure constant defines visual transparency of grapheme, Science 320 (2008) 1308.
[41] J.M. Dawlaty, S. Shivaraman, J. Strait, P. George, M. Chandrashekhar, F. Rana, M.G. Spencer, D. Veksler, Y.Q. Chen, Measurement of the optical absorption spectra of epitaxial graphene from terahertz to visible, Appl. Phys. Lett. 93 (2008) 131905.
[42] J.C. Yu, J.G. Yu, W.K. Ho, Z.T. Jiang, L.Z. Zhang, Effects of F-doping on the photocatalytic activity and microstructures of nanocrystalline TiO_2 powders, Chem. Mater. 14 (2002) 3808–3816.
[43] Y.C. Qiu, S.F. Leung, Q.P. Zhang, C. Mu, B. Hua, H. Yan, S.H. Yang, Z.Y. Fan, Nanobowl optical concentrator for efficient light trapping and high-performance organic photovoltaics, Chin. Sci. Bull. 60 (2015) 109–115.
[44] G.X. Tong, F.T. Liu, W.H. Wu, C.L. Tong, R. Qiao, H.C. Guo, Facile bubble-assisted evaporation-induced assembly of high-density arrays of Co_3O_4 nano/microlotus leaves: fluorescent properties, drug delivery, and biocompatibility, CrystEngComm 16 (2014) 1645–1651.
[45] G.X. Tong, F.F. Du, Y. Liang, Q. Hu, R.N. Wu, J.G. Guan, X. Hu, Polymorphous ZnO complex architectures: selective synthesis, mechanism, surface area and Zn-polar plane-codetermining antibacterial activity, J. Mater. Chem. B 1 (2013) 454–463.
[46] Q. Hu, G.X. Tong, W.H. Wu, F.T. Liu, H.S. Qian, D.Y. Hong, Selective preparation and novel microwave electromagnetic characteristics of polymorphous ZnO architectures made from a facile one-step ethanediamine [en]-assisted hydrothermal approach, CrystEngComm 15 (2013) 1314–1323.
[47] F.F. Du, G.X. Tong, C.L. Tong, Y. Liu, J.Q. Tao, Selective synthesis and shape-dependent microwave electromagnetic properties of polymorphous ZnO complex architectures, J. Mater. Res. 29 (2014) 649–656.
[48] S.G. Kumar, K.S.R.K. Rao, Zinc oxide based photocatalysis: tailoring surface-bulk structure and related interfacial charge carrier dynamics for better environmental applications, RSC Adv. 5 (2015) 3306–3351.
[49] J. Tauc, A. Menth, States in the gap, J. Non-Cryst. Solids 8 (1972) 569–585.
[50] B. Weng, M.Q. Yang, N. Zhang, Y.J. Xu, Toward the enhanced photoactivity and photostability of ZnO nanospheres via intimate surface coating with reduced graphene oxide, J. Mater. Chem. A 2 (2014) 9380–9389.
[51] M.S. Wang, L.X. Jiang, E.J. Kim, S.H. Hahn, Electronic structure and optical properties of $Zn(OH)_2$: LDA + U calculations and intense yellow luminescence, RSC Adv. 5 (2015) 87496–87503.
[52] X.L. Wu, G.G. Siu, C.L. Fu, H.C. Ong, Photoluminescence and cathodoluminescence studies of stoichiometric and oxygen-deficient ZnO films, Appl. Phys. Lett. 78 (2001) 2285–2287.
[53] M.Q. Yang, B. Weng, Y.J. Xu, Improving the visible light photoactivity of In_2S_3-graphene nanocomposite via a simple surface charge modification approach, Langmuir 29 (2013) 10549–10558.
[54] Y. Sun, S.R. Wilson, D.I. Schuster, High dissolution of strong light emission of carbon nanotubes in aromatic amine solvents, J. Am. Chem. Soc. 123 (2001) 5348–5349.
[55] V. Subramanian, E.E. Wolf, P.V. Kamat, Catalysis with TiO_2/gold nanocomposites: effect of metal particle size on the fermi level equilibration, J. Am. Chem. Soc. 126 (2004) 4943–4950.
[56] P. Nordlander, The ring: a leitmotif in plasmonics, ACS Nano 3 (2009) 488–492.
[57] U. Kreibig, M. Vollmer, Optical Properties of Metal Clusters, vol. 25, Springer-Verlag, Berlin Germany, 1995, pp. 13–201.
[58] E.M. Larsson, J. Alegret, M. Käll, D.S. Sutherland, Sensing characteristics of NIR localized surface plasmon resonances in gold nanorings for application as ultrasensitive biosensors, Nano Lett. 7 (2007) 1256–1263.
[59] J. Aizpurua, P. Hanarp, D.S. Sutherland, M. Käll, G.W. Bryant, F.J. García de Abajo, Optical properties of gold nanorings, Phy. Rev. Lett. 90 (2003) 057401.
[60] V. Giannini, R. Rodríguez-Oliveros, J.A. Sánchez-Gil, Surface plasmon resonances of metallic nanostars/nanoflowers for surface-enhanced raman scattering, Plasmonics 5 (2010) 99–104.
[61] C.D. Andrea, J. Bochterle, A. Toma, C. Huck, F. Neubrech, E. Messina, B. Fazio, O.M. Marago, E.D. Fabrizio, M.L.D.L. Chapelle, P.G. Gucciardi, A. Picci, Optical nanoantennas for multiband surface-enhanced infrared and Raman spectroscopy, ACS Nano 7 (2013) 3522–3531.
[62] P. Alonso-González, P. Albella, F. Golmar, L. Arzubiaga, F. Casanova, L.E. Hueso, J. Aizpurua, R. Hillenbrand, Visualizing the near-field coupling and interference of bonding and anti-bonding modes in infrared dimer nanoantennas, Opt. Express 21 (2013) 1270–1280.
[63] S. Kawata, Y. Inouye, P. Verma, Plasmonics for near-field nano-imaging and superlensing, Nat. Photonics 3 (2009) 388–394.
[64] J.X. Low, B. Cheng, J.G. Yu, M. Jaroniec, Carbon-based two-dimensional layered materials for photocatalytic CO_2 reduction to solar fuels, Energy Storage Mater. 3 (2016) 24–35.
[65] G.X. Tong, Y. Liu, T. Wu, Y.C. Ye, C.L. Tong, High-quality elliptical iron glycolate nanosheets: selective synthesis and chemical conversion into Fe_xO_y nanorings, porous nanosheets, and nanochains with enhanced visible-light photocatalytic activity, Nanoscale 7 (2015) 16493–16503.
[66] G.X. Tong, J.G. Guan, Z.D. Xiao, X. Huang, Y. Guan, In-situ generated gas bubble-assisted modulation of the morphologies, photocatalytic and magnetic properties of ferric oxide nanostructures synthesized by thermal decomposition of iron nitrate, J. Nanopart Res. 12 (2010) 3025–3037.
[67] S.G. Kumar, K.S.R.K. Rao, Comparison of modification strategies towards enhanced charge carrier separation and photocatalytic degradation activity of metal oxide semiconductors (TiO_2, WO_3 and ZnO), Appl. Surf. Sci. 391 (2017) 124–148.